New Journal of Physics
The open access journal at the forefront of physics

Deutsche Physikalische Gesellschaft DPG IOP Institute of Physics

Introducing artificial length scales to tailor magnetic properties

To cite this article: J Fassbender *et al* 2009 *New J. Phys.* **11** 125002

New Journal of Physics
The open-access journal for physics

Introducing artificial length scales to tailor magnetic properties

J Fassbender[1,3], **T Strache**[1], **M O Liedke**[1], **D Markó**[1], **S Wintz**[1], **K Lenz**[1], **A Keller**[1], **S Facsko**[1], **I Mönch**[2] **and J McCord**[2]
[1] Institute of Ion Beam Physics and Materials Research, Forschungszentrum Dresden-Rossendorf, PO Box 51 01 19, D-01314 Dresden, Germany
[2] Leibniz Institute for Solid State and Materials Research IFW Dresden, PO Box 27 01 16, D-01171 Dresden, Germany
E-mail: J.Fassbender@fzd.de

New Journal of Physics **11** (2009) 125002 (19pp)
Received 24 April 2009
Published 11 December 2009
Online at http://www.njp.org/
doi:10.1088/1367-2630/11/12/125002

Abstract. Magnetism is a collective phenomenon. Hence, a local variation on the nanoscale of material properties, which act on the magnetic properties, affects the overall magnetism in an intriguing way. Of particular importance are the length scales on which a material property changes. These might be related to the exchange length, the domain wall width, a typical roughness correlation length, or a length scale introduced by patterning of the material. Here we report on the influence of two artificially created length scales: (i) ion erosion templates that serve as a source of a predefined surface morphology (ripple structure) and hence allow for the investigation of roughness phenomena. It is demonstrated that the ripple wave length can be easily tuned over a wide range (25–175 nm) by varying the primary ion erosion energy. The effect of this ripple morphology on the induced uniaxial magnetic anisotropy in soft magnetic Permalloy films is studied. Only below a ripple wavelength threshold ($\approx$60 nm) is a significant induced magnetic anisotropy found. Above this threshold the corrugated Permalloy film acts as a flat film. This cross-over is discussed in the frame of dipolar interactions giving rise to the induced anisotropies. (ii) Ion implantation through a lithographically defined mask, which is used for a magnetic property patterning on various length scales. The resulting magnetic properties are neither present in non-implanted nor in homogeneously implanted films. Here new insight is gained by the comparison of different stripe patterning widths ranging from 1 to 10 μm. In addition, the appearance of more complicated

---

[3] Author to whom any correspondence should be addressed.

magnetic domain structures, i.e. spin-flop domain configurations and head-on domain walls, during hard axis magnetization reversal is demonstrated. In both cases the magnetic properties, the magnetization reversal process as well as the magnetic domain configurations depend sensitively on the artificially introduced length scale.

Contents

1. Introduction

In order to fulfil the continuously exploding demand for larger storage capacities, smaller devices, faster data transfer rates at negligible energy consumption the roadmap of IT technology is heading toward real nanoscale devices. In the past, this has always been achieved by improving nanopatterning technology. However, now we are at the crossroads where fundamentally new physical effects arise due to quantization and interaction phenomena. Also roughness phenomena, even on the atomic scale, might govern the overall performance of the devices. Hence, due to nanopatterning, materials with completely new properties are at the horizon. In order to understand the underlying effects a systematic variation of roughness and feature size is crucial. Thin magnetic films are good model systems to investigate these effects since not only a topographic patterning of the magnetic films is possible but also a systematic crossover from unpatterned to property-patterned, e.g. the magnetic moment is varied locally, to topographically patterned structures can be investigated. Hence interaction phenomena can gradually be switched off. Investigations of this kind are still at an early stage. Still, near future applications are envisaged, which include magneto-resistive and magnetic domain wall devices as well as magnetic thin film materials with optimized hysteresis. In the following, an introduction to this field of research is provided along with selected experimental results.

If a typical roughness periodicity or patterning size approaches intrinsic material length scales like the exchange length or domain wall width in ferromagnetic materials, the corresponding properties are dramatically affected. For example, in thin ferromagnetic films shape anisotropy favors an in-plane magnetized state. If now a sinusoidal surface morphology of the ferromagnetic film is assumed the magnetization tends to orient always parallel to the local surface in order to avoid the creation of stray fields, which costs energy. In order to do so the direction of the magnetization changes locally. However, direct exchange coupling between neighboring spins favors a parallel alignment and hence circumvents a too rapid change of the magnetization direction. In thin ferromagnetic films Néel-walls, which consist of a narrow domain wall core and a rather long range tail, define the intrinsic length scales [1]. The domain wall core w_{core} can be approximated by

$$w_{\mathrm{core}} = \sqrt{\frac{A}{K_{\mathrm{u}} + K_{\mathrm{d}}}}, \tag{1}$$

with A the exchange constant, K_{u} the uniaxial anisotropy and $K_{\mathrm{d}} = J_{\mathrm{S}}^2/2\mu_0$ the domain wall stray field energy contribution [1]. The larger the saturation polarization J_{S} or anisotropy K_{u} the smaller the domain wall core width w_{core}. For $d = 10\,\mathrm{nm}$ thick polycrystalline Permalloy films, a typical core width of $w_{\mathrm{core}} \approx 10\,\mathrm{nm}$ is found. The domain wall tail is approximated by

$$w_{\mathrm{tail}} \approx 0.56 \frac{d K_{\mathrm{d}}}{K_{\mathrm{u}}}, \tag{2}$$

i.e. the tails influence the magnetic behavior across $w_{\mathrm{tail}} \approx 10\,\mu\mathrm{m}$ lateral distances [1]. For typical 3d ferromagnets like Fe, Co and Ni, the saturation polarization and/or the anisotropy are larger than for Permalloy, which correspondingly leads to smaller intrinsic length scales, which are more difficult to reach by patterning techniques. Hence, we restrict ourselves to the discussion of Permalloy films throughout the present paper.

Similar arguments hold if it is not the surface morphology that is changed but the local magnetic properties, e.g. magnetic anisotropy, magnetic moment, saturation magnetization or Curie temperature, by broad beam ion implantation through lithographically defined masks. If the modified areas are large enough, an individual switching of the magnetization in areas with different magnetic properties occurs. Hence, during magnetization reversal, domain walls are created at predefined locations at the boundary between areas with modified and unmodified magnetic properties. Since the areas are large, the distance between adjacent domain walls is large and hence the interaction between them is negligible. However, if the modified areas shrink in size, the separation between the domain walls becomes smaller and hence their interaction increases. Finally, if the magnetic patterning is performed on a lateral scale of the order of the domain wall core width, no domain walls can be formed and the creation of an effective medium is expected. This effective medium describes inhomogeneous materials in which the description of the microscopic magnetic properties of both constituents can be replaced within effective medium theory by effective magnetic parameters, which rely on the properties of the individual constituents and in addition on the geometric configuration.

The paper is divided into two experimental sections that address the morphology-induced length scales in section 2 and the length scales associated with magnetic property patterning in section 3. Both sections start with a paragraph introducing the method of patterning. Subsequently, the corresponding magnetic properties are discussed. Finally, a summary of the observed phenomena is provided.

2. Morphology-induced effects

Surface and interface roughnesses or modulations play a significant role for a large number of properties of thin magnetic films. For example, it is possible to induce magnetic anisotropy contributions due to a periodic surface modulation. The microscopic origin can be extrinsic due to dipolar stray fields, as well as intrinsic due to spin–orbit coupling phenomena at monoatomic steps. The relative contribution of both microscopic effects to the macroscopically measurable

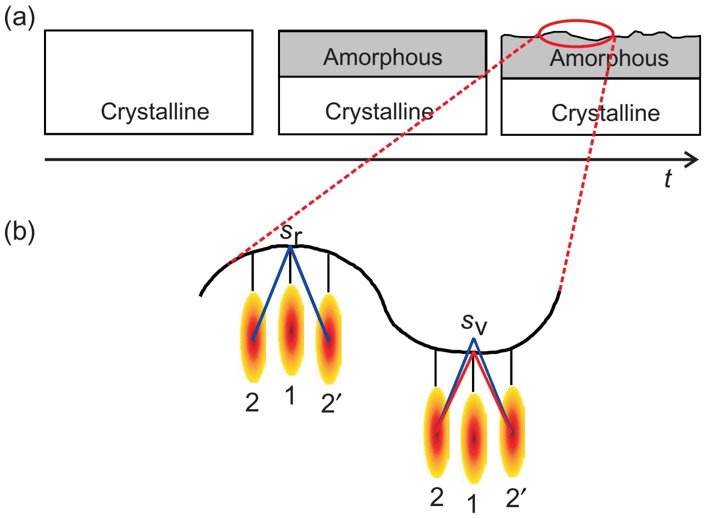

Figure 1. (a) Sketch of the temporal evolution of the ion erosion process. (b) Sketch of the energy distribution (color-coded) of impinging ions on a modulated surface. 1, 2 and 2′ denote the different ions. The corresponding distances between the impacts and the surface on the ridge, s_r and in the valley, s_v are indicated by blue and red lines, respectively.

material properties depends sensitively on the film crystallinity, the exchange length, and the modulation wavelength and amplitude. The latter two can be varied by the use of ion-eroded semiconductor substrates and determined quantitatively. This allows for a detailed investigation of the relevant length scales associated with a periodic surface modulation in order to induce magnetic anisotropies. In section 2.1, a short overview of self-organized pattern formation during ion erosion is presented. In the subsequent section 2.2, the induced magnetic anisotropies are presented as a function of modulation wavelength.

2.1. Ion erosion for the creation of a predefined substrate/film morphology

The surface morphology can be systematically modified by means of ion erosion [2]. In addition to smoothing or to statistically roughening surfaces by ion irradiation also the creation of self-organized periodic patterns is possible [3, 4]. The characteristics of these periodic structures is primarily determined by the ion energy, the angle of incidence of the ions and the temperature of the irradiated surface. The understanding of the periodic pattern formation due to ion erosion dates back to 1988 when Bradley and Harper [5] discovered an inherent mechanism directly emerging from the sputter process itself. Starting from the Sigmunds sputter theory [6], explaining the surface roughening due to a curvature-dependent ion erosion rate that is larger in valleys than on ridges, they introduced surface diffusion as a counteracting process. In a certain parameter regime, the interplay between both processes can lead to the formation of periodic patterns.

In figure 1, the ion erosion process is sketched. In figure 1(a), the temporal evolution of the surface during ion erosion of a semiconductor single crystal is shown. In the initial stages of ion erosion, the near-surface region is amorphized. Subsequently, a statistical roughness with valleys and ridges appears. In figure 1(b), a detail of such a surface morphology is shown.

In order to understand the mechanism responsible for the larger erosion rate in the valleys, one has to consider the energy loss of an impinging ion (shown for perpendicular incidence). In a certain depth (depending on the primary energy of the ions) most energy is deposited. The energy distribution is considered as being Gaussian (as sketched by the color-coded ellipses). The erosion rate is determined by the energy deposition at the surface of the ridges, s_{r} and of the valleys, s_{v}. If one first considers the energy deposition of the first ion (ion 1) impinging on the surface the energy deposition is inversely proportional to the distance of the maximum energy deposition to the surface. This distance and hence energy deposition is the same irrespective of the position of impact, s_{r} or s_{v}. However, if neighboring impacts are considered (ions 2 and 2′) the energy deposition at position s_{r} and s_{v}, respectively, depends on the curvature of the surface. The distance to the surface position s_{r} (s_{v}) is indicated by blue (red) lines. From the comparison of red and blue lines on the right-hand side, it becomes immediately clear that more energy is deposited and hence the erosion rate is larger at position s_{v} than at s_{r}. Consequently, a rough surface becomes unstable during ion erosion and the roughness increases. In contrast, thermally activated or ion-induced surface diffusion [3] leads to a smoothing of the surface. Under certain circumstances the interplay between both counteracting processes leads to the creation of a periodic pattern. Depending on the symmetry of the ion irradiation either dot or ripple structures are created. Based on the model of Bradley and Harper [5], a nonlinear partial differential equation that clarifies the most important aspects of the pattern formation has been derived [7]:

$$\frac{\partial h(x,y,t)}{\partial t} = -v_0 + \nu_x \frac{\partial^2 h}{\partial x^2} + \nu_y \frac{\partial^2 h}{\partial y^2} + \frac{\zeta_x}{2}\left(\frac{\partial h}{\partial x}\right)^2 + \frac{\zeta_y}{2}\left(\frac{\partial h}{\partial y}\right)^2 - D_{\mathrm{eff}}\nabla^2(\nabla^2 h). \tag{3}$$

This differential equation describes the temporal evolution of the surface morphology during continuous erosion. v_0 denotes the constant erosion rate of the planar surface, and the coefficients ν_x and ν_y are the so-called negative surface tension coefficients, which describe the surface instability during ion erosion. D_{eff} denotes the sum of thermally and ion-induced surface diffusion processes and the nonlinear terms proportional to ζ_x and ζ_y incorporate the dependence of the local erosion rate on the surface slopes. By means of a linear stability analysis of the equation the wavelength of the periodic pattern λ can be derived and connected to the mean penetration depth of the ions $a(E)$ and sputter rate $Y(E)$ at a given primary energy E:

$$\lambda = 2\pi\sqrt{\frac{2D_{\mathrm{eff}}}{\mathrm{Min}\mid \nu_x, \nu_y \mid}} \propto \frac{a(E)}{\sqrt{Y(E)}}. \tag{4}$$

In figure 2(a), a numerical integration of equation (3) is presented and compared with an atomic force microscopy (AFM) image of an ion-eroded Si surface. The integration has been performed by using a difference scheme on a grid of 200 × 200 lateral nodes with $\Delta x = \Delta y = 1$ and $\Delta t = 0.01$. The coefficients used in the current simulation were $\nu_x = -1$, $\nu_y = -0.3$, $\zeta_x = 0.1$, $\zeta_y = 0.05$ and $D_{\mathrm{eff}} = 1$. The image shown in figure 2(a) corresponds to a simulation time $t = 55$. If appropriate deposition conditions are chosen during metal film deposition on top of such an ion-eroded Si surface, the surface morphology is completely transferred to the metallic film as shown by a cross-sectional transmission electron microscopy (TEM) micrograph.

Important for the present investigation is the possibility to vary the modulation wavelength. Since the mean ion penetration depth and the sputter rate depend on the primary energy of the ions a square root energy dependence is expected in the low ion energy regime (0.1–1 keV) and a linear dependence in the medium energy range (5–50 keV). This dependence has been verified

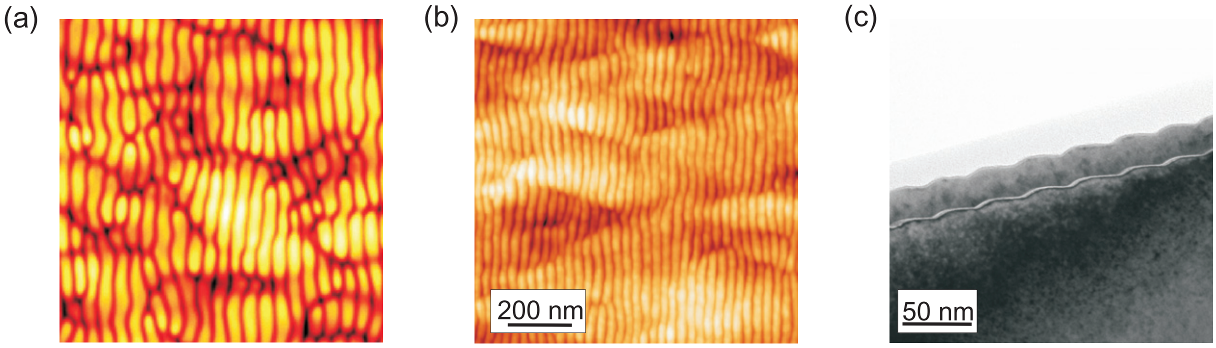

Figure 2. (a) Simulation of the surface morphology created by low-energy ion erosion based on the model presented in the text. The x and y scales depend only on the simulation parameters and can be rescaled arbitrarily. (b) AFM image of the surface morphology of an ion-eroded Si surface. (c) Cross-sectional TEM image of the ion-eroded surface covered with a metallic film. A perfect replication of the surface pattern into the metal film surface is observed by comparing the surface and interface morphology displayed in (c).

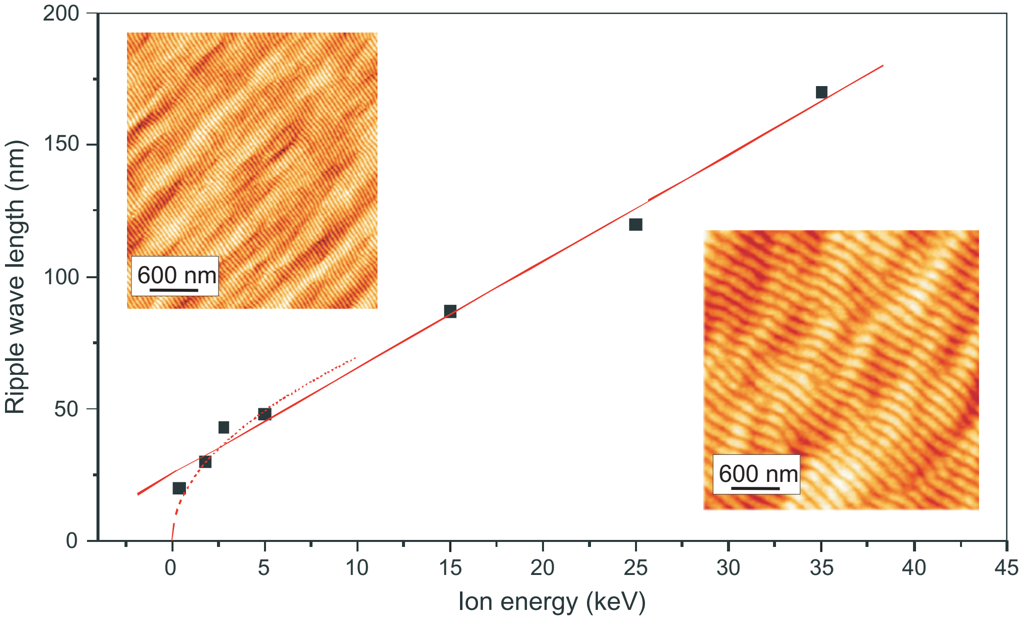

Figure 3. Ripple wavelength as a function of primary ion energy. The insets show two AFM images for ion erosion with a primary energy of 5 and 25 keV. Both image scan sizes are identical for a better comparison.

experimentally in the low-energy regime, especially for Si [8] and GaSb [9], and also in the medium energy range [10]. The surface roughness and hence the modulation amplitude of the periodic pattern increase following either an exponential or power-law behavior as a function of ion fluence. However, saturation is reached quickly [8]. On a Si surface typical aspect ratios are 0.2. Consequently, this method allows for a creation of periodic Si patterns with a wavelength ranging from 10 to 200 nm and a modulation amplitude ranging from 1 to 20 nm (see figure 3).

2.2. Ripple-induced magnetic anisotropies

Magnetic anisotropies caused by the breaking of translational invariance have been investigated since decades [11]. Initially surface and interface anisotropy contributions and hence the crossover from three dimension (3D) to 2D have been experimentally investigated [11]–[13] and theoretically described [14, 15]. In addition to the well-known shape anisotropy originating from dipolar effects the spin–orbit coupling is modified due to the reduced atomic coordination at the surface. Hence additional magnetic anisotropy contributions appear. Subsequently, anisotropy contributions arising from atomic step edges, mainly originating from vicinal miscut single crystals, have been addressed (crossover from 2D to 1D dimensional) [16]–[23]. However, in some investigations [24, 25] ion erosion has already been used for the creation of an anisotropic step density distribution. The step edge contribution leads to an induced uniaxial magnetic anisotropy. Again this anisotropy contribution is explained in terms of a modified spin–orbit coupling. Dipolar contributions as an origin of these magnetic anisotropies are only discussed to less extent. In all experiments mentioned so far, single crystalline epitaxial nanostructures or ultrathin films with often atomically sharp interfaces are investigated. Hence, on the one hand morphology-induced anisotropy contributions are always superimposed by magneto-crystalline or strain-induced anisotropy contributions and on the other hand, interface roughness phenomena are negligible. The understanding of these model systems is already advanced. We face a completely different situation if polycrystalline films are considered. In ‘real’ systems, interface roughness effects are often crucial for the explanation of many magnetic parameters, e.g. magnetic anisotropies [26]–[30], magnetic damping [31]–[35], exchange bias [36]–[38], coupling phenomena [39, 40] and magneto-resistance [41, 42]. Many of these publications are more theoretical and in the few experimental investigations the influence of interface roughnesses can hardly be correlated with the associated modification of magnetic properties. The main reason for this is that surface and interface roughnesses could not be varied in a precise manner. For the quantification of the roughness usually the root-mean-square (RMS) roughness, w_{rms}, is used. The corresponding correlation length is typically neither considered nor varied. Based on a theory by Schlömann [26] a uniaxial surface modulation with an amplitude w_{rms} and a wavelength λ leads to a uniaxial in-plane anisotropy of

$$K_2^{\mathrm{dip}} = 2\pi M_S^2 \frac{\pi w_{\mathrm{rms}}^2}{\lambda D} \tag{5}$$

with the saturation magnetization M_{S} of the ferromagnetic film of thickness D. In contrast to the described step-edge anisotropy, which originates from spin–orbit coupling, this anisotropy is solely caused by dipolar stray fields generated due to the surface morphology. From equation (5) it becomes immediately clear that in addition to the RMS-roughness the roughness correlation length has to be considered. In addition also the exchange constant A of the ferromagnetic material, which determines together with the magnetic anisotropy the exchange correlation length, is important. Implicitly, in equation (5) it is assumed that the magnetization of the modulated film is homogeneously oriented, i.e. the effect of the exchange constant dominates over the morphology-induced anisotropy and hence no local modulations of the magnetization direction are possible. A more comprehensive theory is given by Arias and Mills [29].

In the following, the effect of a periodic surface patterning on the magnetic anisotropy will be demonstrated. As a model system a 9 nm thick Permalloy film is grown by molecular beam epitaxy on top of the $\mathrm{SiO_2}$ ripple templates of various modulation wavelength. Details of

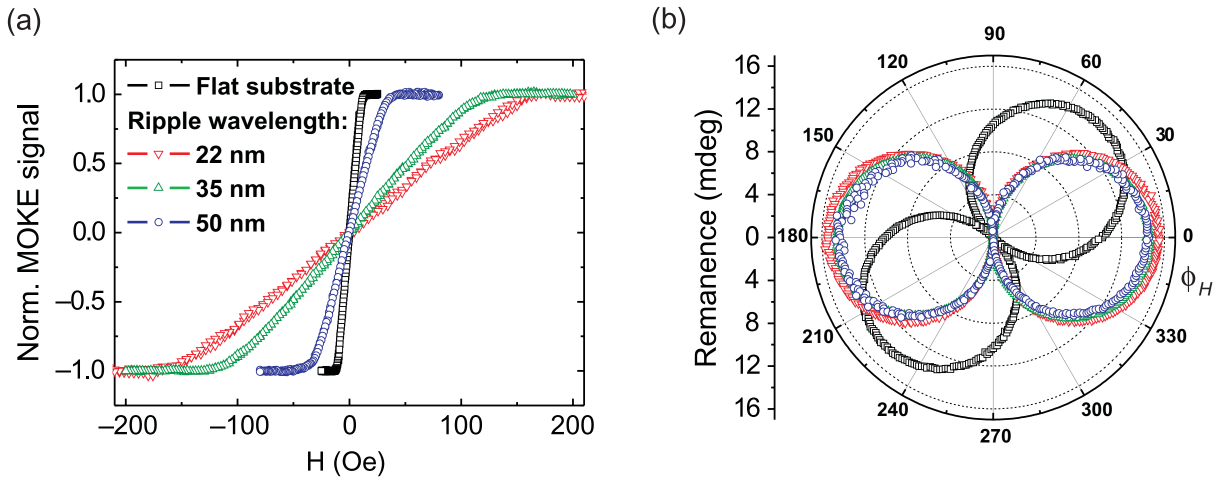

Figure 4. (a) Hard axis magnetization reversal investigated by MOKE for Permalloy films prepared on substrates with various ripple wavelengths as indicated. (b) Angular dependence of the remanence for the same films as in (a).

the template preparation are reported elsewhere [43]. In order to achieve a perfect replication of the ripple morphology into the metallic film (cf figure 2(c)) a 5 nm thick Cr buffer is used. In figure 4(a), the hard axis magnetization reversal curves investigated by means of longitudinal magneto-optic Kerr effect (MOKE) magnetometry are shown for films deposited on a ripple template with a wavelength of 22 nm (red), 35 nm (green), 50 nm (blue), and compared with flat films (black). It becomes immediately clear that the saturation field, i.e. the applied magnetic field at which the magnetic moment reaches saturation, strongly depends on the ripple wavelength. The shorter the wavelength the larger the saturation field and hence the induced magnetic anisotropy. In order to demonstrate the uniaxial nature of the induced anisotropy in figure 4(b) the angular dependence of the remanence is shown. For $\phi_{\mathrm{H}} = 0$, the applied field is oriented along the edge of the substrate. In this orientation, the magnetic field is applied parallel to the ripples. However, for the flat film the direction of the uniaxial anisotropy, which is given by the magnetic field applied during deposition, is not correlated with the substrate edge, as can be seen from the angular dependence of the flat film that is rotated with respect to the sample edge.

The induced magnetic anisotropy is also investigated by means of vector network analyzer ferromagnetic resonance (VNA-FMR) [44, 45] measurements, which allows for the variation of frequency and applied magnetic field. The resonance frequency f is shown as a function of applied magnetic field in figure 5 for the easy (full symbols) and hard (open symbols) axis of the ferromagnetic films deposited on different ripple templates. Assuming only in-plane uniaxial anisotropy the FMR frequency is given by

$$f = \frac{\gamma}{2\pi}\sqrt{(H + H_{\mathrm{ani}})(H + H_{\mathrm{ani}} + M_{\mathrm{S}})}, \tag{6}$$

with γ the gyromagnetic ratio. The solid lines shown in figure 5 are the corresponding fits of the anisotropy field H_{ani} to the experimental data. Making use of the equation

$$K_2 = \tfrac{1}{2} M_{\mathrm{S}} H_{\mathrm{ani}}, \tag{7}$$

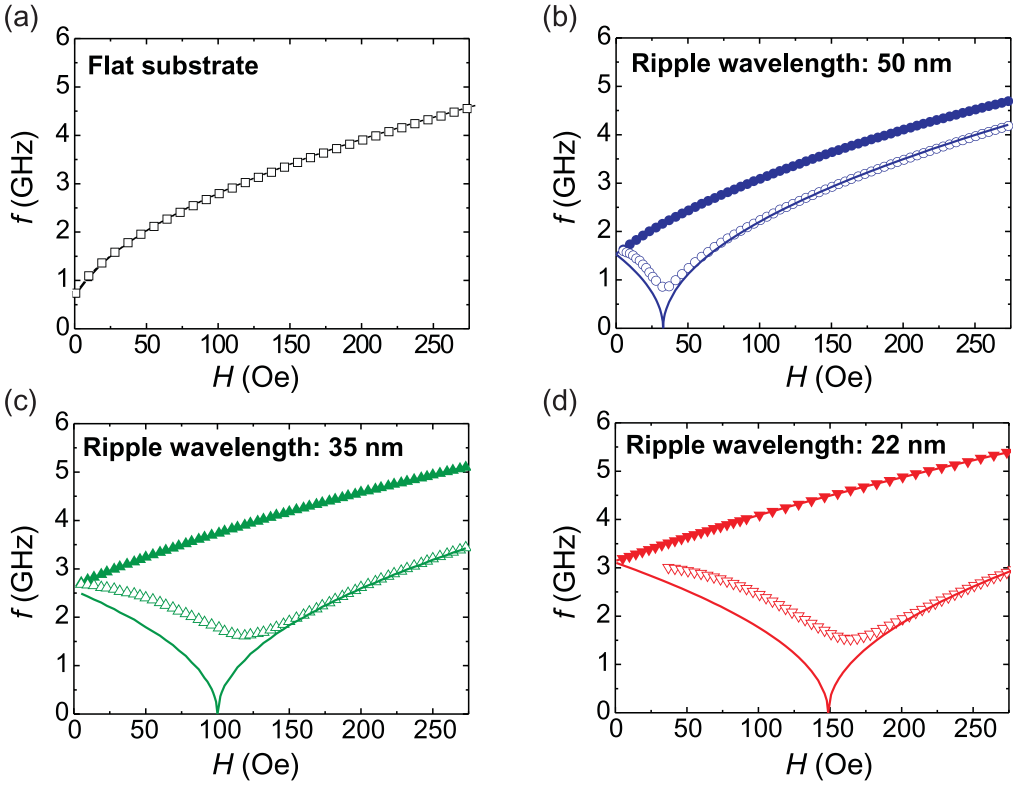

Figure 5. Easy (full symbols) and hard axis (open symbols) FMR results for Permalloy films prepared on substrates with various ripple wavelengths as indicated. The solid lines are fits based on a model described in the text.

one can easily determine the induced uniaxial anisotropy constant, K_2. This anisotropy constant is plotted as a function of ripple wavelength in figure 6. A strong increase of the uniaxial anisotropy is observed for decreasing ripple wavelength below about 60 nm. Above 60 nm ripple wavelength, the magnetization of the Permalloy film can always orient parallel to the local surface and hence no difference with respect to a nominally flat Permalloy film is observed. In contrast, below a ripple wavelength of 60 nm the magnetization cannot follow the surface morphology and stray fields are generated, which are the source of the induced magnetic anisotropy. However, the dependence of the induced uniaxial anisotropy on the ripple wavelength does not follow a simple $1/\lambda$ dependence as expected from Schlömann's theory [26]. One reason for this discrepancy is the simplification that in this theory the magnetization is strictly oriented in-plane and no local variation in magnetization direction is included. However, this assumption holds only for very short ripple wavelength. For larger ripple wavelength Schlömann's theory provides only an upper limit for the induced uniaxial anisotropy.

3. Magnetic property patterning

In the previous section, the lateral length scale that affects the magnetic properties was given by the wavelength of the ripple structures and hence a purely morphological length scale. Due

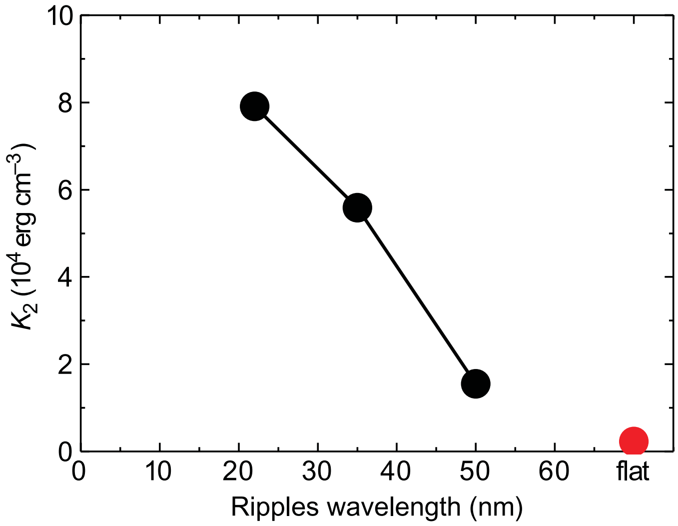

Figure 6. Induced uniaxial anisotropy K_2 as a function of ripple wavelength.

to the self-organization process very small structures, in the range of a few tens of nanometers, were achieved in this bottom-up patterning approach. In this section, a completely different approach will be presented, which also demonstrates impressively that materials modification on the nanoscale can dramatically alter the overall properties of a material system and hence lead to magnetic properties, which cannot be achieved by traditional material synthesis methods. Here the method of choice relies on a top-down patterning approach, which allows for the property patterning of the material system with the intention to circumvent topography effects to the largest possible extent. The main idea is to modify the magnetic properties, e.g. the magnetic moment or the Curie temperature, of a thin magnetic film locally. In section 3.1, it will be shown that this can easily be done by means of ion implantation methods. Hence magnetically softer and harder regions, which are in direct lateral contact by means of exchange coupling, can be realized. Thereby completely new domain walls and domain configurations, which are not possible in conventional thin films, are created at predefined locations. With further miniaturization the domains vanish and an effective material with new properties, neither observed in fully implanted nor in the non-implanted films, is created. These are so-called hybrid materials. Depending on the patterning sizes an independent switching of the individual areas or a strongly coupled magnetization reversal behavior can be observed. The major goal will be to correlate the artificially generated magnetic domain structure with magnetization reversal behavior.

3.1. Ion-induced modification of magnetic properties

Starting with the paper by Chappert *et al* [46] a large number of publications have addressed the modification of magnetic properties by means of ion irradiation. Typically, light ion irradiation was used in order to modify the mutual interface between ferromagnetic and non-ferromagnetic thin films. Also ordering and disordering processes in binary alloys have been investigated. For a review see [47]. The modification of single ferromagnetic films by means of ion implantation has been addressed to less extent. In early papers mostly Ga implantation from a focused ion beam (FIB) system was used to modify the magnetic properties locally [48]–[51]. Hence

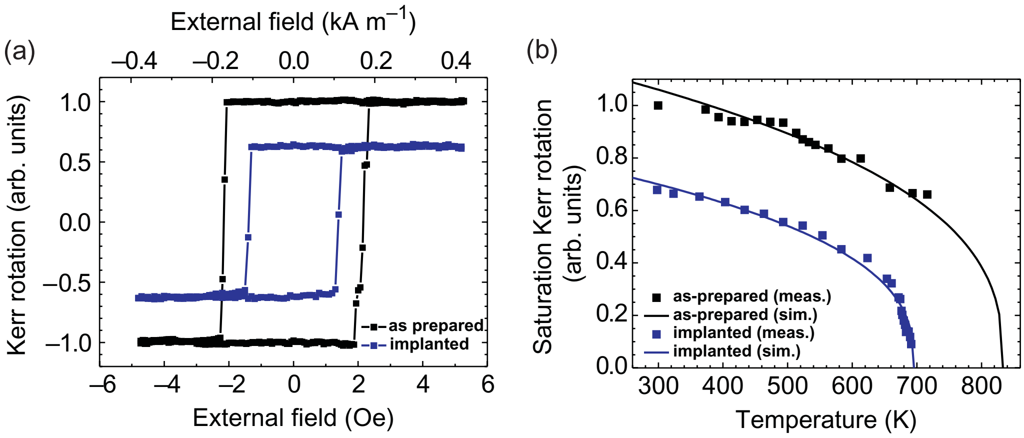

Figure 7. (a) Easy axis magnetization reversal loops investigated for an as-grown Permalloy film (black) and a homogeneously Cr implanted (1×10^{16} ions cm^{-2}) Permalloy film (blue). (b) Temperature dependence of the magnetic moment of both films. The solid lines are simulations of the temperature dependence assuming a Curie temperature of 833 and 695 K, respectively, using equation (8).

typically magnetic domain imaging is performed with less emphasis on the mechanism leading to the magnetic material modification. Subsequently also 3d metals have been implanted with the intention to either lower the Curie temperature [52]–[56], or to modify the magnetic anisotropy [57, 58]. In the case of rare-earth implantation also a modification of the magnetic damping behavior could be achieved [59]. For a review on magnetic patterning by means of ion irradiation and implantation, see [60].

In the following, we restrict ourselves to the model system of Cr implantation into Permalloy. From the bulk phase diagram [61] it is well known that Cr doping leads to a reduction of the Curie temperature, T_C and hence at a given temperature to a reduction of the magnetic moment $m(T)$. The basic modifications in structure and magnetism upon Cr implantation into Permalloy have been reported elsewhere [55]. The sample system x nm $Ni_{80}Fe_{20}/SiO_2/Si$; x ranging from 20 to 30 nm, has been prepared by means of magnetron sputter deposition. During deposition a magnetic field was applied in the film plane in order to set the easy axis of the uniaxial anisotropy. For the implantation a fixed low fluence of 1×10^{16} ions cm^{-2} at a primary energy of either 15 or 30 keV was chosen. From TRIDYN simulations [62] and Rutherford backscattering (RBS) investigations the sputter erosion depth is determined to be below 4 nm.

In figure 7(a), the easy axis hysteresis loops are shown for Permalloy films as-grown and after homogeneous Cr ion implantation with a fluence of 1×10^{16} ions cm^{-2}. A reduction of the magnetic moment after ion implantation to approximately 65% of the initial value is observed by the reduced MOKE amplitude of the implanted film. In order to check if this reduction is due to a reduced Curie temperature, the temperature dependence of the magnetic moment was determined for both films. In figure 7(b), the magnetic moment determined from the amplitude of the MOKE signal is shown as a function of measurement temperature. The solid lines are simulations based on

$$m(T) = m(0)\left(1 - \frac{T}{T_C}\right)^{\beta} \tag{8}$$

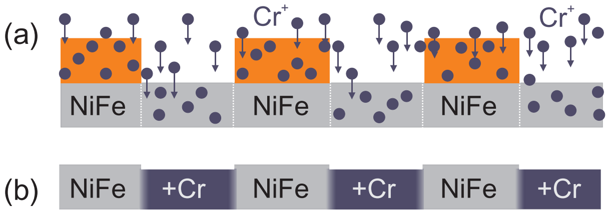

Figure 8. Sketch of the fabrication procedure of a hybrid material. (a) The resist allows the ions to stop completely before entering the Permalloy film. (b) After resist removal a lateral hybrid material system is formed.

with $\beta = 0.364$, assuming a 3D Heisenberg model [63]. For the homogeneously implanted Permalloy film, the Curie temperature is determined to be 695 K. The experimental data of the as-grown Permalloy film are consistent with a bulk Curie temperature of 833 K. Due to the limited temperature range no experimental data above 730 K could be taken. In the next step, a hybrid material is created by a lateral combination of as-grown and implanted Permalloy using local ion implantation. The goal of section 3.2 will be to evaluate the influence of different patterning sizes ranging from 10 μm down to 1 μm for these hybrid materials.

3.2. Magnetization reversal and domain configurations for different patterning sizes

For the creation of a hybrid material first a resist is spin-coated on top of the Permalloy film that is sufficiently thick to completely stop the ions during implantation. Subsequently, optical lithography is used to define lines within the resist structure. After development narrow lines of various widths between 10 and 1 μm are opened. The separation of the lines is always chosen the same as the width of the stripes themselves. During broad beam implantation, the Permalloy film is only implanted in areas where the resist has been removed prior to implantation (see figure 8). Finally, the resist is removed and a full film structure composed of implanted and non-implanted areas is realized. Subsequently, the magnetic properties of the integral structures are investigated by means of inductive magnetometry at a frequency of 10 Hz. The magnetic domain structure during magnetization reversal is investigated by means of Kerr microscopy with varying in-plane magnetic field in the longitudinal mode [1]. First results demonstrating the creation of a lateral exchange spring structure have been published in [64].

In order to address the influence of different length scales in lateral magnetic patterning three different stripe widths are chosen. In the case of 10 μm (1 μm) wide stripes, the patterning dimension should be larger (smaller) than the Néel wall widths, including the laterally extended Néel wall tail. The 4 μm wide stripes represent a transition regime between both extrema. In the top row of figure 9, the easy axis magnetization reversal loops are shown. For the 10 μm wide stripes, slight rotational processes in the magnetization reversal close to coercivity are observed which are not present in the unpatterned film. The coercive field is nearly the same (cf figure 7). In contrast for the narrower stripe widths the coercivity has increased significantly with respect to the as-deposited as well as to the homogeneously Cr implanted film. The reversal along the stripe axis manifests itself in a distinct two-step process, which is even more pronounced for the 1 μm wide stripes. Also the coercive field, which is determined by the second switching event, is further increased for the reduced stripe width. In addition, the magnetization approaches saturation at higher magnetic field values. Note the different field scales in figures 9(b) and (c).

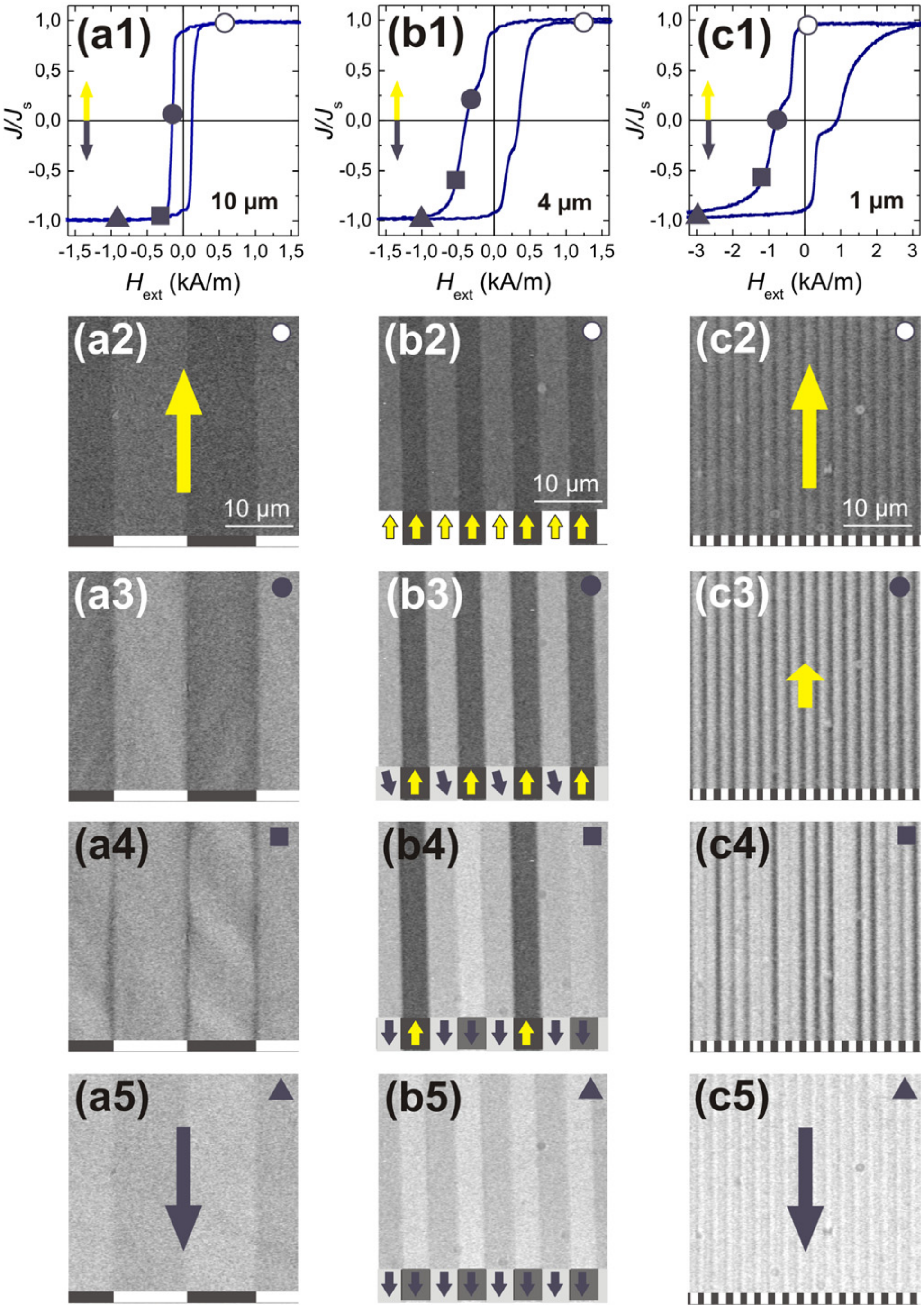

Figure 9. Comparison of the easy axis (parallel to stripes) magnetization reversal behavior of a magnetically patterned Permalloy film and the corresponding magnetic domain structure for three different stripe patterning sizes: (a) 10 μm, (b) 4 μm and (c) 1 μm. In the top row, the easy axis magnetization reversal loops are shown. In the subsequent rows, Kerr microscopy images showing the magnetic domain configuration are shown for applied field values as indicated by the symbols in the image and the corresponding loop. The implanted (non-implanted) areas are indicated in white (black) at the bottom of each image.

However, the reversal mechanisms and the local processes cannot be identified from the hysteresis loops.

Hence, magneto-optical domain imaging is employed. Images of the magnetic domain evolution during reversal along the stripe axis are displayed in rows 2–5 of figure 9 for the different stripe widths. In saturation (second and fifth rows) the stripes can still be observed, since the lower magnetic moment in the implanted areas lead to a reduction in magneto-optical Kerr intensity. For the 10 μm wide stripes, a multi-domain structure occurs in the implanted as well as in the non-implanted regions during magnetization reversal. An interaction between both areas is only visible close to the mutual lateral interfaces at applied magnetic fields close to saturation (see figure 9(a4)). This situation changes considerably if the 4 and 1 μm wide stripes are considered. Here, the initial switching process occurs by the reversal of the sample's irradiated parts. With reduction of field, the magnetization in the low moment irradiated regions first rotates and then rapidly switches by conjunctly occurring domain wall motion through the stripes (figure 9(b2)→(b3) and (c2)→(c3)). This result is consistent with the relative height of the steps observed in hysteresis loops displayed in figures 9(b1) and (c1), considering the reduction of magnetic moment with Cr implantation. Narrowly spaced 180° domain walls are formed after completion of this process. The position and density of these domain walls are directly determined by the induced periodicity of the magnetization modulation, which can be immediately used for domain wall magneto-resistive devices. The second part of the reversal is dominated by independent switching events of a single stripe's magnetization. Note the individual switching of stripes in figures 9(b3)–(b5) and (c3)–(c5). In contrast to the first switching event, the second switching process occurs gradually over a wide field range. This is related to a wide distribution of domain wall annihilation fields, necessary for the switching process in each magnetic wire. The switching mechanism parallel to the stripe direction, which proceeds via head-on domain wall motion, is very similar for these two stripe widths. As discussed before, one of the major differences in comparison to isolated stripes is the direct exchange coupling between the neighboring ferromagnetic materials. Therefore, in the demagnetized state of the 4 μm wide stripes a strong correlation of magnetization between adjacent stripes with the formation of extended quasi-domain structures becomes visible (not shown; see [64]). The correlation of the spins is much higher than in the case of pure magneto-static interactions as observed in conventionally patterned stripe arrays [65].

Next we address the magnetization reversal process for a magnetic field aligned perpendicular to the stripe axis, i.e. the hard axis magnetization reversal. For the 10 μm wide stripes (see figure 10(a1)) more rotational processes are observed compared with the case where the field is aligned parallel to the stripe axis. However, the coercivity is the same for an applied field parallel and perpendicular to the stripe axis. In contrast to the head-on domain wall motion dominated magnetization reversal process in the narrower stripes observed for the applied field oriented parallel to the stripe axis, the magnetization reversal perpendicular to the stripe axis is mostly determined by magnetization rotation processes. For the hard axis, magnetization reversal for the 4 μm wide stripes a bimodal magnetization behavior is observed (see figure 10(b1)). In contrast for the 1 μm wide stripes the hysteresis exhibits a behavior similar to a hard axis loop of a full film sample (see figure 10(c1)). Note the different field scales in figures 10(b) and (c). No sign of a two-step or an inhomogeneous magnetization reversal can be identified. Concurrently, the coercivity is close to zero and thus significantly smaller than for the wider stripes.

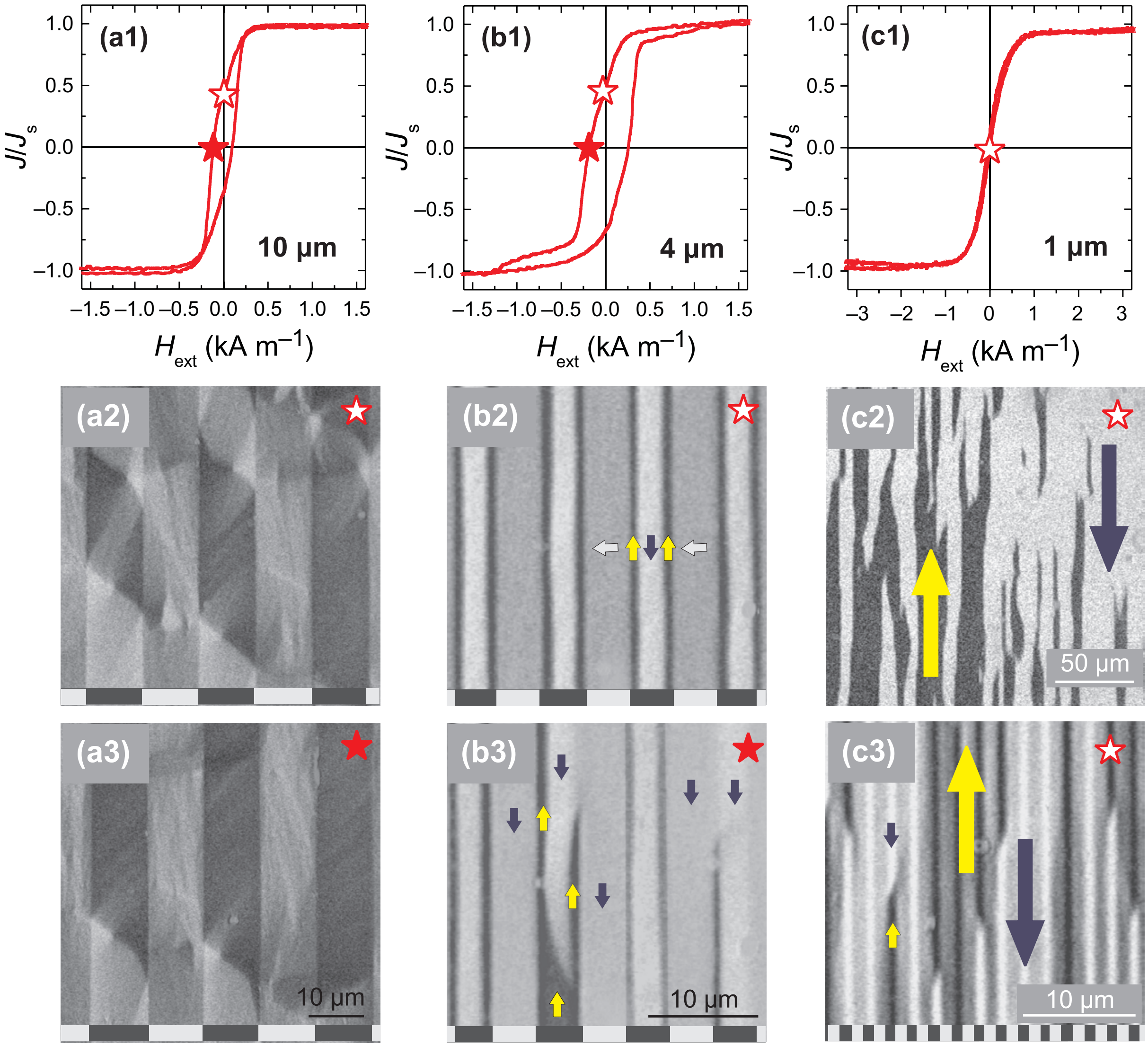

Figure 10. Comparison of the hard axis (perpendicular to stripes) magnetization reversal behavior of a magnetically patterned Permalloy film and the corresponding magnetic domain structure for three different stripe patterning sizes: (a) 10 μm, (b) 4 μm and (c) 1 μm. In the top row, the hard axis magnetization reversal loops are shown. In the subsequent rows, Kerr microscopy images showing the magnetic domain configuration at remanence and coercivity are shown as indicated by the symbols in the image and the corresponding loop. For the 1 μm stripes, a low magnification (c2) and high-resolution (c3) image is shown. The implanted (non-implanted) areas are indicated in white (black) at the bottom of each image.

In order to address the microscopic origin of this magnetization reversal behavior the magnetic domain configuration during magnetization reversal is investigated. For the 10 μm wide stripes a complicated domain structure is observed. In the non-implanted areas, the magnetization is aligned perpendicular to the original field direction with mostly vortex or cross-tie walls separating the regions of oppositely aligned magnetization direction. No correlation between the borders of the magnetic patterns and the domain wall alignment is found. The domain structure within the non-implanted areas extends also to the low magnetic moment implanted areas. However, less contrast is observed in these regions, since the magnetization is still mainly aligned with respect to the original magnetization direction.

For the 4 μm wide stripes, the magnetization distribution in remanence and close to coercivity is displayed in figures 10(b2) and (b3), respectively. Both images show an intriguing magnetization configuration. Starting from saturation at the borders of the higher moment, non-implanted stripes domains are nucleated due to magneto-static interactions. With further reduction of the field, a buckled domain pattern is formed in the non-implanted stripes. As seen in figure 10(b2), the magnetization inside the implanted areas is still aligned almost parallel with the initial field direction. The magnetization inside the non-implanted stripes then further transforms into a structure with an anti-parallel alignment of magnetizations perpendicular to the applied field direction, forming a three-domain state, reminiscent of a spin-flop configuration. This structure then dissolves by head-on domain wall motion through the stripes (see the stripe on the right-hand side of the image in figure 10(b3)). Close to coercivity head-on domain structures in the center of the stripe and head-on border domain walls are observed (figure 10-b3). As opposed to the non-implanted parts, the magnetization within the implanted stripes is homogeneous and changes by magnetization rotation only. The increased domain wall density together with observed complicated head-on domain wall movement necessary to annihilate the domain walls lead to the increased coercivity relative to the 10 μm case.

Reducing the stripe width to smaller dimensions, the domain wall-induced effects diminish. The magnetic domain structure of figure 10(c2) resembles that of a ferromagnetic full film with uniaxial magnetic anisotropy after hard axis demagnetization. This observation is consistent with the corresponding magnetization loop presented in figure 10(c1). The extended quasi-domains, the absence of head-on domain wall motion during the almost purely rotation magnetization process, and the increase of effective anisotropy lead to a reduction of coercivity relative to the 10 μm case. Due to the limited resolution of the low magnification objective used for this observation no sub-structure inside the quasi-domains can be obtained. High-resolution imaging (figure 10(c3)) elucidates a possible complicated internal magnetization pattern. Quasi-domains with parallel and anti-parallel alignment of adjacent magnetization states become visible. Extended regions with a parallel alignment of magnetization directions across several stripes can be identified. The circumference of these quasi-domains consists of stripe boundaries and head-on domain walls. No additional formation of domain walls aligned parallel to the stripe axis as for the 4 μm wide stripes can be forced. Moreover, at the position of the head-on domain wall structures, a change of magnetization in adjacent stripes is observed in figure 10(c3). Apparently, the head-on domain walls relieve a part of their magnetostatic energy by a partial magnetization rotation in the adjacent stripes, which is impossible in isolated magnetic stripes.

4. Summary

It has been demonstrated that artificially introduced length scales can dramatically affect the magnetic properties of ultrathin magnetic films. In the case of short wavelength surface and interface modulations, a large induced uniaxial magnetic anisotropy was observed, which can be up to two orders of magnitude larger than the intrinsic anisotropy of the material system itself.

By varying the modulation wavelength it can be demonstrated that shorter wavelengths lead to larger effects. This can be understood considering the fact that exchange interactions favor a parallel alignment of adjacent spins and hence the magnetization cannot change its direction on very short length scales that would be required in order to keep the magnetization always parallel to the local surface. This was also the key ingredient for the observed modifications in the case of hybrid materials. Here it was especially important that an interaction of adjacent domain walls governed the magnetization reversal behavior to a large extent. For large patterning sizes, a nearly unaffected magnetization reversal was observed, whereas for shrinking patterning sizes quasi-domain states and intriguing new magnetic domain phenomena were observed, which are only related to the magnetic property patterning. In future work, the fundamental limits of shrinking the size of the modified areas in these magnetic property-patterned structures will be explored.

Acknowledgments

We thank R Mattheis and R Kaltofen for the Permalloy sample supply and A Mücklich for the TEM inspection of the ripple structure. Special thanks go to W Möller, L Schultz and O G Schmidt for continuous support. Financial support by the Deutsche Forschungsgemeinschaft (FA 314/3 and FA 314/6) is greatly appreciated.

References

[1] Hubert A and Schäfer R 1998 *Magnetic Domains* (Berlin: Springer)
[2] Murty M V R 2002 *Surf. Sci.* **500** 523
[3] Makeev M A, Cuerno R and Barabasi A L 2002 *Nucl. Instrum. Methods Phys. Res.* B **197** 185
[4] Chan W L and Chason E 2007 *J. Appl. Phys.* **102** 121301
[5] Bradley R M and Harper J M E *J. Vac. Sci. Technol.* A **6** 2390
[6] Sigmund P 1973 *J. Mater. Sci.* **8** 1545
[7] Cuerno R and Barabasi A L 1995 *Phys. Rev. Lett.* **74** 4746
[8] Ziberi B, Frost F, Hoche T and Rauschenbach B 2005 *Phys. Rev.* B **72** 235310
[9] Facsko S, Kurz H and Dekorsy T 2001 *Phys. Rev.* B **63** 165329
[10] Karmakar P and Ghose D 2005 *Nucl. Instrum. Methods Phys. Res.* B **230** 539
[11] Gradmann U 1974 *Appl. Phys.* A **3** 161
Gradmann U 1974 *J. Magn. Mater.* **54** 733
[12] Heinrich B and Cochran J F 1993 *Adv. Phys.* **42** 523
[13] Johnson M T, Bloemen P J H, den Broeder F J A and de Vries J J 1996 *Rep. Prog. Phys.* **59** 1409
[14] Néel L 1954 *J. Phys. Rad.* **15** 376
[15] Chappert C and Bruno P 1988 *J. Appl. Phys.* **64** 5736
[16] Berger A, Linke U and Oepen H P 1992 *Phys. Rev. Lett.* **68** 839
[17] Chen J and Erskine J L 1992 *Phys. Rev. Lett.* **68** 1212
[18] Chuang D S, Ballentine C A and O'Handley R C 1994 *Phys. Rev.* B **49** 15084
[19] Weber W, Bischof A, Allenspach R, Back C H, Fassbender J, May U, Schirmer B, Jungblut R M, Güntherodt G and Hillebrands B 1996 *Phys. Rev.* B **54** 4075
[20] Kawakami K, Escorcia-Aparicio E J and Qiu Z Q 1996 *Phys. Rev. Lett.* **77** 2570
[21] Dhesi S, van der Laan G, Dudzik E and Shick A B 2001 *Phys. Rev. Lett.* **87** 067201
[22] Gambardella G, Dallmeyer A, Maiti K, Malagoll M C, Eberhardt W, Kern K and Carbone C 2002 *Nature* **416** 301

[23] Rusponi S, Cren T, Weiss N, Epple M, Buluschek P, Claude L and Brune H 2003 *Nat. Mater.* **2** 546
[24] Moroni R, Sekiba D, Buatier de Mongeot F, Gonella G, Baragno C, Mattera L and Valbusa U 2003 *Phys. Rev. Lett.* **91** 167207
[25] Bisio F, Moroni R, Buatier de Mongeot F, Canepa M and Mattera L 2006 *Phys. Rev. Lett.* **96** 057204
[26] Schlömann E 1970 *J. Appl. Phys.* **41** 1617
[27] Bruno P 1988 *J. Appl. Phys.* **64** 3153
[28] Zhao Y-P, Palasantzas G, Wang G-C and De Hosson J Th M 1999 *Phys. Rev.* B **60** 1216
[29] Arias R and Mills D L 1999 *Phys. Rev.* B **59** 11871
[30] Wolfe J H, Kawakami R K, Ling W L, Qiu Z Q, Arias R and Mills D L 2001 *J. Magn. Magn. Mater.* **232** 36
[31] Arias R and Mills D L 1999 *Phys. Rev.* B **60** 7395
[32] McMichael R D, Twisselmann D J and Kunz A 2003 *Phys. Rev. Lett.* **90** 227601
[33] Dobin Yu A and Victora R H 2004 *Phys. Rev. Lett.* **92** 257204
[34] Maranvill B B, Mallet J, Moffat T P, McMichael R D, Chen A P and Egelhoff W F Jr 2005 *J. Appl. Phys.* **97** 10A721
[35] Craus C B, Palasantzas G, Chezan A R, De Hosson J Th M, Boerma D O and Niesen L 2005 *J. Appl. Phys.* **97** 013904
[36] Thomas L, Negulescu B, Dumont Y, Tessier M, Keller N, Wack A and Guyot M 2002 *J. Appl. Phys.* **93** 6838
[37] Liu C, Yu C, Jiang H, Shen L, Alexander C and Mankey G J 2000 *J. Appl. Phys.* **87** 6644
[38] Liedke M O, Liedke B, Keller A, Hillebrands B, Mücklich A, Facsko S and Fassbender J 2007 *Phys. Rev.* B **75** 220407
[39] Kudrnovsky J, Drchal V, Turek I, Sob M and Weinerberg P 1996 *Phys. Rev.* B **53** 5125
[40] Körner M, Lenz K, Liedke M O, Strache T, Keller A, Facsko S, Mücklich A and Fassbender J 2009 *Phys. Rev.* B, submitted
[41] Fullerton E E, Kelly D M, Guimpel J, Schuller I K and Bruynseraede Y 1992 *Phys. Rev. Lett.* **68** 859
[42] Schrag B D *et al* 2000 *Appl. Phys. Lett.* **77** 2373
[43] Keller A, Roßbach S, Facsko S and Möller W 2008 *Nanotechnology* **19** 135303
[44] Kalarickal S S, Krivosik P, Wu M, Patton C E, Schneider M L, Kabos P, Silva T J and Nibarger J P 2006 *J. Appl. Phys.* **99** 093909
[45] Neudecker I, Woltersdorf G, Heinrich B, Okuno T, Gubbiotti G and Back C H 2006 *J. Magn. Magn. Mater.* **307** 148
[46] Chappert C *et al* 1998 *Science* **280** 1919
[47] Fassbender J, Ravelosona D and Samson Y 2004 *J. Phys. D: Appl. Phys.* **37** R179
[48] Ozkaya D L, Langford R M, Chan W L and Petford-Long A K 2002 *J. Appl. Phys.* **91** 9937
[49] Konings S, Miguel J, Luigjes J, Schlatter H, Luigjes H, Goedkoop J and Gadgil V 2005 *J. Appl. Phys.* **98** 054306
[50] McGrouther D and Chapman J N 2005 *Appl. Phys. Lett.* **87** 022507
[51] Konings S, Miguel J, Goedkoop J, Camarero J and Vogel J 2006 *J. Appl. Phys.* **100** 033904
[52] Folks L, Fontana R E, Gurney B A, Childress J R, Maar S, Katine J A, Baglin J E E and Kellock A J 2003 *J. Phys. D: Appl. Phys.* **36** 2601
[53] Fassbender J and McCord J 2006 *Appl. Phys. Lett.* **88** 252501
[54] Fassbender J, Mücklich A, Potzger K and Möller W 2006 *Nucl. Instrum. Methods* B **248** 343
[55] Fassbender J, von Borany J, Mücklich A, Potzger K, Möller W, McCord J, Schultz L and Mattheis R 2006 *Phys. Rev.* B **73** 184410
[56] Gupta R, Ansari R, Khandelwal A, Fassbender J and Gupta A 2008 *Nucl. Instrum. Methods* B **266** 1407
[57] McCord J, Mönch I, Fassbender J, Mücklich A, Quandt E and Gerber A 2009 *J. Phys. D: Appl. Phys.* **42** 055006
[58] Martin N *et al* 2009 *Appl. Phys. Lett.* **94** 062506
[59] Dasgupta V, Litombe N, Bailey W E and Bakhru H 2006 *J. Appl. Phys.* **99** 08G312

[60] Fassbender J and McCord J 2008 *J. Magn. Magn. Mater.* **320** 579
[61] Bozorth R M 2003 *Ferromagnetism* (Hoboken, NJ: IEEE Press)
[62] Möller W, Eckstein W and Biersack J P 1988 *Comput. Phys. Commun.* **51** 355. The TRIDYN code is available at http://www.fzd.de
[63] Le Guillou J C and Zinn-Justin J 1977 *Phys. Rev. Lett.* **39** 95
[64] McCord J, Schultz L and Fassbender J 2008 *Adv. Mater.* **20** 2090
[65] Theis-Bröhl K, Toperverg B P, Leiner V, Westphalen A, Zabel H, McCord J, Rott K and Brückl H 2005 *Phys. Rev.* B **71** 020403